

Submitted to Astrophysical Journal

## **A new catalog of photometric redshifts in the Hubble Deep Field <sup>1</sup>**

Alberto Fernández-Soto<sup>2,3</sup>, Kenneth M. Lanzetta <sup>3</sup>, and Amos Yahil<sup>3</sup>

---

<sup>1</sup>Based on observations taken with the NASA/ESA Hubble Space Telescope, which is operated by AURA under NASA contract NAS5-26555 and at the Kitt Peak National Observatory, which is operated by AURA under cooperative agreement with the NSF.

<sup>2</sup>Department of Astrophysics and Optics, School of Physics, University of New South Wales, Kensington-Sydney, NSW 2052, Australia

<sup>3</sup>Department of Physics and Astronomy, State University of New York at Stony Brook, Stony Brook, NY 11794–3800

## ABSTRACT

Using the newly available infrared images of the Hubble Deep Field in the  $J$ ,  $H$ , and  $K$  bands and an optimal photometric method, we have refined a technique to estimate the redshifts of 1067 galaxies. A detailed comparison of our results with the spectroscopic redshifts in those cases where the latter are available shows that this technique gives very good results for bright enough objects ( $AB(8140) < 26.0$ ). From a study of the distribution of residuals ( $\Delta z_{\text{rms}}/(1+z) \approx 0.1$  at all redshifts) we conclude that the observed errors are mainly due to cosmic variance. This very important result allows for the assessment of errors in quantities to be directly or indirectly measured from the catalog. We present some of the statistical properties of the ensemble of galaxies in the catalog, and finish by presenting a list of bright high-redshift ( $z \approx 5$ ) candidates extracted from our catalog, together with recent spectroscopic redshift determinations confirming that two of them are at  $z = 5.34$  and  $z = 5.60$ .

*Subject headings:* Cosmology: Observations – Galaxies: Distances and Redshifts – Galaxies: Photometry – Galaxies : Statistics

## 1. Introduction

The Hubble Deep Field (HDF) image (Williams *et al.* 1996) is the deepest view of the universe yet obtained. The image was acquired by the Hubble Space Telescope (HST) using the Wide Field Planetary Camera 2 (WFPC2) over a period of ten consecutive days in December 1995, yielding unprecedented sensitivity and angular resolution over a  $3 \times 3$  arcmin<sup>2</sup> portion of the sky. The image was acquired through the F300W, F450W, F606W, and F814W broad-band filters (of central wavelengths near 2940, 4520, 5940, and 7920 Å), allowing for the possibility of assigning redshifts to objects detected in the image on the basis of broad-band photometry. This so called photometric redshift technique was originally applied to galaxies detected in other fields by various authors (see, e.g., Loh & Spillar 1986; Connolly *et al.* 1995), with remarkably successful results. Several groups have by now applied the photometric redshift technique to galaxies detected in the HDF, each using a slightly different approach, and it was recently verified that all groups obtain essentially correct results in the limit of bright, moderate-redshift ( $z < 1.4$ ) galaxies (see Hogg *et al.* 1998 and references therein).

In our first work (Lanzetta, Yahil & Fernández-Soto 1996, hereafter LYF), we described our version of the photometric redshift technique. Using a maximum-likelihood analysis applied to precise photometry and a selection of galaxy spectral templates (including templates of E/S0, Sbc, Scd, and Irr galaxies), we presented a catalog of 1683 objects in the HDF complete to magnitude  $AB(8140) = 28.0$ . For each object, we listed a position, magnitude, estimated redshift, and estimated spectral type. We showed that the redshifts were mostly reliable, in the sense that more than 85% were essentially correct ( $\Delta z_{\text{rms}} \approx 0.15$ ) when compared with the then-available redshifts determined by means of spectroscopic observations. Nevertheless, some issues were raised about the validity of the photometric redshift technique, mainly concerning the possibility of confusion between high-redshift galaxies and heavily-reddened low-redshift galaxies.

Since our first work, infrared images of the HDF were acquired through the  $J$  (1.2  $\mu\text{m}$ ),  $H$  (1.65  $\mu\text{m}$ ), and  $K$  (2.2  $\mu\text{m}$ ) broad-band filters (Dickinson *et al.* 1998). Although these images are not as deep as the optical images, they are of great utility for the photometric analysis because they augment by more than a factor of three the available wavelength coverage. This additional information is important for two reasons: First, it can help to resolve the redshift degeneracy observed in some cases by LYF—where the interpretation of breaks in the spectra of some galaxies is made difficult because low-redshift Balmer (and other) discontinuities are confused with high-redshift Lyman discontinuities. Second, it can help to distinguish high-redshift galaxies from heavily-reddened low-redshift galaxies by measuring or constraining the observed-frame infrared spectral energy distributions.

The infrared images differ qualitatively from the optical images in that the spatial resolution of the infrared images is about an order of magnitude lower than the spatial resolution of the optical images. For this reason, it is essential that the photometry of the infrared images be performed in a very careful way, taking as much profit as possible of the valuable information

that has already been extracted from the optical images. Here we use the optical images to create model spatial profiles that are fitted to the infrared images in order to measure optimal infrared fluxes and uncertainties. Even in cases where the galaxies are not bright enough to be detected in the infrared images, we are able to establish firm upper limits to the infrared emission. These limits have direct consequences on the redshift likelihood functions, and they also strictly limit the reddening that can be affecting the galaxies under consideration.

In this paper, we present our new analysis. We explain the changes we have made to our technique in order to incorporate the infrared images, and we present a new catalog of photometric redshifts. The catalog includes optimal infrared fluxes—or upper limits—and uncertainties as well as photometric redshift estimates for 1067 objects. We also present a comparison of our results with new spectroscopic observations that have become available since our first work.

The organization of this paper is as follows: Section 2 presents the data. Section 3 describes the object detection and photometry procedures, with particular attention to the infrared flux measurements. The method used to obtain the estimated redshifts is presented in § 4. The final catalog is presented in § 5 and compared to spectroscopically determined redshifts in § 6. We discuss some relevant properties of the distribution of galaxies in § 7, and review our main conclusions in § 8.

## 2. Data

The optical images were acquired by HST in December 1995 using WFPC2 and the F300W, F450W, F606W, and F814W filters (Williams *et al.* 1996). Reduced versions of the images were made available for public access in January 1996. The physical format of the optical images is  $4096 \times 4096$  pixel<sup>2</sup> at a plate scale of  $0.04$  arcsec pixel<sup>−1</sup>, which corresponds to an angular area of  $\approx 3 \times 3$  arcmin<sup>2</sup>. Throughout this work, we refer to coordinates with respect to the Mosaic version of the images, which were created by Mark Dickinson and Richard Hook from the Version 2 images provided by the STScI team, and to the filters F300W, F450W, F606W and F814W as *U*, *B*, *V*, and *I* respectively.

The infrared images were obtained by Kitt Peak National Observatory 4 m telescope in April 1996 using the IRIM camera and standard *J*, *H*, and *K* filters (Dickinson *et al.* 1998). Reduced versions of the images were made available for public access in November 1996. The physical format of the infrared images is  $1024 \times 1024$  pixel<sup>2</sup> at a plate scale of  $0.16$  arcsec pixel<sup>−1</sup>, which corresponds to an angular area of  $\approx 3 \times 3$  arcmin<sup>2</sup>. The infrared images are registered to the same coordinate grid as the optical images.

## 3. Object detection and photometry

### 3.1. Object detection

We use the SExtract source extraction code (Bertin & Arnouts 1996) to detect objects in the F814W image. Details of the procedure are described by LYF96. At this stage, the object list contains 2323 objects with *best* total  $AB(8140)$  magnitudes down to  $\approx 30$ . Total magnitudes labeled by SExtract as *best* are first measured as aperture magnitudes and then corrected for the effect of neighboring objects and the flux lost in pixels outside the aperture. We will use these *best* magnitudes to define the completeness limits of our catalog as well as in the studies that depend on magnitudes of individual objects (like the galaxy counts and other studies sketched in Section 7.), but the calculations described in this and the following Section will be based on aperture magnitudes as defined in Section 3.2..

It is known that the edges of the Wide Field Camera images as well as the Planetary Camera image are of poorer quality than the bulk of the Wide Field Camera images. In our previous work, we trimmed the image borders to avoid contamination by spurious sources. In the present work, we instead define two different zones of two different depths in order not to exclude some bright objects that are located in the previously trimmed area, some of which have spectroscopic redshifts available.

The inner part of the image (hereafter zone 1, or Z1) is the deeper zone, which is cut to a magnitude limit of  $AB(8140) = 28.0$ . To this limit, there are 946 galaxies spread over an angular area of  $3.92 \text{ arcmin}^2$ . The outer part of the image (hereafter zone 2, or Z2)—including the external borders of the Wide Field Camera images and the Planetary Camera image—is the shallower zone, which is cut to a magnitude limit of  $AB(8140) = 26.0$ . To this limit, there are 121 galaxies spread over an angular area of  $1.39 \text{ arcmin}^2$ . Zones Z1 and Z2 are defined in Figure 1.

### 3.2. Photometry

To perform the optical photometry, we repeat the analysis described by LYF. This analysis is based on the definition of an aperture for every object by means of the segmentation map given by the application of SExtract to the F814W image. The segmentation map marks the pixels of every object detected in the F814W image, which corresponds to an isophotal aperture of surface brightness limit  $\mu_{AB(8140)} = 26.1 \text{ arcsec}^{-2}$ .

Given the apertures, we calculate the observed flux of every object in every optical image by summing the fluxes within the apertures and subtracting the backgrounds determined in boxes surrounding the objects. To assess errors in the flux values, we calculate the  $3 \times 3$  data covariance matrix of every image, because, as is described by Williams *et al.* (1996), the drizzling algorithm applied to the images to improve the spatial resolution produces correlations between adjacent

pixels (stronger between immediate neighbors and less important, but still significant, in diagonal directions). We account for this effect in the calculation of the photometric errors using the data covariance matrix, that has the net effect of increasing the flux errors that would be measured otherwise. This increase is determined essentially by the values of the correlation between neighboring pixels, with a correction that depends on the shape and size of the object—number of pixels within the measured aperture.

Using apertures fixed by the F814W image assures that the same portion of every object is measured in every filter, hence this method is preferable to any other variable-aperture technique for this work. But this approach cannot be easily adapted to photometry of the infrared images. The difference between the infrared images and the optical images is, of course, that the ground-based infrared images are of significantly lower spatial resolution than the space-based optical images. To account for this difference, we apply a procedure that yields essentially optimal infrared photometry of every object detected in the optical images.

We make the single assumption that the spatial profiles of objects detected in the F814W image—which is observed at the extremely high spatial resolution provided by HST—are good tracers of the spatial profiles at observed-frame infrared wavelengths. This assumption is plausible for the following reasons: For objects of low redshift, observed-frame infrared wavelengths correspond to rest-frame infrared or red wavelengths, at which galaxy morphology is not a sensitive function of wavelength. For objects of high redshift, typical galaxy angular sizes are much less than the seeing profile of the infrared images (LYF), so the objects are almost always unresolved by the infrared images. Together, these effects make the above-mentioned assumption reasonable in all cases of interest for the present analysis. Moreover, *BVRIHK* observations of spiral galaxies by de Jong & van der Kruit (1994) and de Jong (1996) show no significantly different profiles in the optical and infrared bands.

First we determine the shapes of the point spread functions of the infrared images by fitting Gaussian profiles to stars detected in the images. The variation of the point spread functions with position on the field is taken into account by fitting quadratic polynomials to the point spread function FWHM as functions of the distance to the center of the field. Table 1 shows the polynomial coefficients obtained from these fits, from which it can be appreciated that this effect must be taken into account in order to perform accurate photometry.

Next, we convolve the F814W image of every object with the appropriate point spread functions in order to obtain models of the infrared spatial profiles in the three infrared bands. We call  $P_i^{(b)}(m, n)$  the model profile of object  $i$  at pixel  $(m, n)$  in infrared band  $b$ , normalized to unit total flux. Using the  $P_i^{(b)}(m, n)$ , we create model images  $M^{(b)}$ , which are linear sums of the profiles of every object in band  $b$ . The profile of every object is multiplied by a flux  $F_i^{(b)}$  in band  $b$ , which is a parameter to be fitted. The individual profiles are summed according to

$$M^{(b)}(m, n) = \sum_{i=1}^{N_{\text{obj}}} F_i^{(b)} P_i^{(b)}(m, n). \quad (1)$$

In order to achieve maximum accuracy in the determination of the fluxes, it is also necessary to obtain a very good estimate of the background and the noise in every image and of its statistical characteristics. To obtain this estimate for the  $i$ th object, we calculate the local background  $B_i^{(b)}$  and  $3 \times 3$  data covariance matrix  $\bar{\sigma}_i^{(b)}$  using all pixels in a box surrounding the object that are not identified as belonging to any source—including of course the object under study. The data covariance matrix is normalized so that its central element  $\bar{\sigma}_i^{(b)}(2, 2)$  is equal to  $\sigma_{\text{loc}}^2$ , the standard deviation of the local distribution of noise values around the source. We then define an *effective*  $\sigma$  for that area to be

$$\sigma_{\text{eff}_i}^{(b)} = \left[ \sum_{i_1, i_2=1}^{i_1, i_2=3} \bar{\sigma}_i^{(b)}(i_1, i_2) \right]^{1/2}, \quad (2)$$

which is actually a slightly conservative overestimate of the real error.

The model image  $M^{(b)}$  is then fitted to the observed infrared image  $I^{(b)}$  by means of a  $\chi^2$  linear minimization technique, rendering the equation

$$\chi^2 = \sum_{m,n} \left[ \frac{I^{(b)}(m,n) - B^{(b)}(m,n) - M^{(b)}(m,n)}{\sigma_{\text{eff}}^{(b)}(m,n)} \right]^2. \quad (3)$$

This requires the resolution of a  $N_{\text{obj}}^2$  matrix which is very sparse, because the only non-zero elements arise at pairs of indices whose related objects overlap. The set of  $N_{\text{obj}}$  equations that minimizes  $\chi^2$  is

$$\frac{\partial \chi^2}{\partial F_i^{(b)}} = 0 \quad (i = 1, \dots, N_{\text{obj}}), \quad (4)$$

which leads to the Hessian matrix of the system:

$$A_{ij}^{(b)} = \frac{\sum_{m,n} P_i^{(b)}(m,n) P_j^{(b)}(m,n)}{\sigma_{\text{eff}_i}^{(b)} \sigma_{\text{eff}_j}^{(b)}}, \quad (5)$$

and the right hand side of the equation:

$$R_i^{(b)} = \frac{\sum_{m,n} P_i^{(b)}(m,n) [I^{(b)}(m,n) - B_i^{(b)}]}{(\sigma_{\text{eff}_i}^{(b)})^2}. \quad (6)$$

In both definitions the indices  $(m, n)$  span the entire image. The result of this procedure is the set of fitted fluxes  $F_i^{(b)}$  and associated uncertainties  $\sigma_{F_i}^{(b)}$  for  $i = 1, \dots, N_{\text{obj}}$ .

### 3.3. Validation tests for the IR photometry

As the procedure we have sketched in this Section is rather complex and, as far as we know, has not been presented before, we consider it necessary to perform some tests on the results to assess the validity of the technique.

A first idea on the goodness of the achieved fit can be obtained by simply having a look at Figure 2, which shows a piece of the  $K$  band image, together with the corresponding F814W image, the  $K$  band model as fitted by our procedure and the residual image. A detailed analysis of the residual image suggests that the infrared PSF might not be perfectly Gaussian, which may produce errors in our photometry. We have checked that these errors are smaller than  $\Delta[AB(22000)] \approx 0.1$  for the brightest objects ( $AB(22000) \approx 18$ ) and smaller than  $\Delta[AB(22000)] \approx 0.2$  for the faintest ones (those with  $AB(22000) \approx 24$ ). In general this systematic error is smaller than the photometric error for all objects with  $AB(22000) \gtrsim 23$ —which is approximately 90% of the catalog.

We now show two tests that are very different in nature and will help us to establish the accuracy of the measured IR fluxes and their associated noise estimates.

### 3.3.1. Infrared photometry of faint objects

Because the optical images are of much higher quality (in terms of depth and spatial resolution) than the infrared images, we can expect a very significative fraction of the objects to have infrared fluxes measured by our technique that are compatible with zero. Having measured a flux  $F_i$  and an associated error  $\sigma_i$  for every one of the objects in any infrared image, we can form the quotients

$$q_i = F_i/\sigma_i \quad (7)$$

which tell us how significantly different from zero every flux is that we measure on the image. Excluding the objects with high values of  $q_i$ , we can concentrate only on the above-mentioned objects whose flux is compatible with zero.

We can use this sample of objects to check that our error analysis has been correct. If that is the case, the distribution of values of  $q_i$  must have two components: First, a normal distribution with mean value  $\bar{q} = 0$  and variance  $\sigma_q = 1$ , that accounts for the fact that a fraction of the flux measurements are completely indistinguishable from zero. Second, a group of positive values that makes the  $q > 0$  side broader, corresponding to measurements of fluxes from weak sources. The relative importance of these two components will depend on the relative depth and spatial resolution of the two images involved (in our case, F814W for the detection of the objects and the infrared image for the flux measurements). Other properties of the images (like the flat-fielding and putative background variations) are not a limiting factor in this analysis, as the quality of both the HST and Kitt Peak images is very good. We decided, in any case, to estimate the background and covariance matrix locally for each object in each band, which makes our analysis even more robust in that sense.



In order to check whether the two components described above appear in our flux distributions and to measure their relative importances, we show in Figure 3 the distributions of  $q_i$  for all three infrared bands, and superimposed on them a Gaussian distribution ( $\bar{q} = 0$ ,  $\sigma_q = 1$ ) whose only free parameter is the normalization level. This normalization is calculated to fit the number of objects *in the negative part of the distribution*, to avoid the influence of those weak positive flux measurements on the positive side of the distribution.

Looking at the  $q < 0$  distributions we can see that there is perfect agreement between the expected and observed distributions. This is proof that the infrared photometric errors are Gaussian and that our estimation of their values is likely correct. The other side of the distribution ( $q > 0$ ) is broadened—as expected—because of the accumulation of positive measurements that correspond to very faint sources.

### 3.3.2. Distribution of the residuals

In order to check that the model light profiles that we are using in our fit are correct, we can study the distribution of the residual intensities in the image that results from subtracting the model from the original image. First, each of the infrared images is divided in two different sectors. The first sector contains all those pixels whose values in the model image are significantly different than zero (using a  $1\sigma_{\text{loc}}$  threshold, with  $\sigma_{\text{loc}}$  being the standard deviation of the local distribution of background values). The second sector contains the rest of the points, i.e., the ones that—according to the model—contain essentially only background noise.

Figure 4 shows in the upper panels the histograms of the pixel intensity distributions—normalized to unit area—in both sectors for all three bands. They are obviously different, as expected, with the intensities in the first sector (continuous line) being higher than the ones in the second (dotted line). This merely shows the fact that the pixels corresponding to the sources, which are those with high intensities, are all in the first group. The dashed lines (corresponding to background pixel intensity distributions) are all consistent with Gaussian noise.

We can now look at the histograms of the intensities corresponding to the same pixels in the residual images (i.e.,  $I^{(b)} - M^{(b)}$ , lower panels of the same Figure). In this case, both distributions are seen to have the same mean value. This indicates that the residual source intensities average to zero which means that our measured fluxes are not biased either towards low or high values. However, we observe in the same panels that the variance around zero is different in the intensity distributions for the first and second sectors. This is expected, as it is due to the fact that we are subtracting the intensities corresponding to the models, but of course we cannot avoid the fact that the noise (essentially Poissonian on the images) is higher where the signal used to be higher.

## 4. Redshift estimation

We estimate the redshift of every object detected in the F814W image from the photometric data using the technique described by LYF, except that here we use seven optical and infrared photometric bands whereas LYF used only four optical photometric bands. The idea is to compare the observed spectral energy distributions (SED) with a grid of model galaxy SEDs (including the effects of intrinsic and intervening absorption) ranging in spectral type and redshift.

### 4.1. Selection of the model spectra

We use as basic galaxy spectra the four spectra templates given by Coleman, Wu & Weedman (1980). They include four different *observed* galaxy types (E/S0, Sbc, Scd, and Irr) and cover the wavelength range 1400-10000 Å. We extrapolate these templates at ultraviolet wavelengths to 912 Å using results of Kinney *et al.* (1993) and at infrared wavelengths up to 25000 Å using spectral evolutionary models of Bruzual & Charlot (1993). We show in Table 2 the parameters we have used to construct the infrared extensions of the templates, as suggested by Pozzetti, Bruzual & Zamorani (1996). Figure 5 shows the four spectra used as input models. We do not include Lyman  $\alpha$  emission in our templates. This is due to the large spread of Lyman  $\alpha$  emission line equivalent widths observed in moderate to high-redshift galaxies—ranging from negative (heavily absorbed profiles) to  $\approx 60$  Å. Even the largest quoted equivalent widths would produce only minor effects in our broad-band photometry except for the putative case of very strong Lyman  $\alpha$  lines in galaxies at  $z \approx 4.1$  or  $z \approx 6.0$ , when the lines would occupy the red end of the F606W or F814W filters respectively. These cases may deserve future studies, specially as the number of spectroscopically confirmed  $z > 4$  galaxies is increased.

Intrinsic neutral hydrogen absorption is incorporated into the models by assuming that galaxies are optically thick to ionizing radiation below the Lyman Limit (912 Å in the galaxy rest frame). This assumption has been verified by Leitherer *et al.* (1995) for nearby starburst galaxies and has been checked in those objects where spectroscopic redshifts are available. Intervening neutral hydrogen absorption is incorporated into the models (as a function of redshift) by adopting the average Lyman  $\alpha$  and Lyman  $\beta$  decrement parameters  $D_A$  and  $D_B$ , as measured by Madau (1995) and Webb (1996). Given that these measurements extend only over the redshift range  $0 < z < 6$ , we extrapolate the values to higher redshifts using a simple polynomial fit passing through Webb (1996) points  $D_A(z = 6) = 0.951$ ,  $D_B(z = 6) = 0.961$  and forcing  $D_A = D_B = 1$  for  $z = 8$ .

We do not include evolutionary corrections in the model spectra because such corrections are very uncertain and would add additional parameters to the model—including, for example, the galaxy ages. We believe, moreover, that the adopted galaxy spectra span a wide enough range

of spectral properties to account for evolution in a purely passive way. However, it is certainly true that distant galaxies with spectral properties significantly different from all present-day galaxies would render a problem for our method. Such cases have not been seen in observations of high-redshift galaxies so far (Cohen *et al.* 1996; Lowenthal *et al.* 1997; Zepf, Moustakas, & Davies 1997; Steidel *et al.* 1996). In the particular case of very high-redshift galaxies, their main spectral feature is the utter lack of flux below  $912(1+z)$  Å and almost complete lack of flux below  $1215(1+z)$  Å. In these cases, other features of the spectra turn out to have close to negligible effect on the redshift estimates, as is demonstrated by the fact that *at high redshifts* our fitting procedure gives almost the same goodness of fit and redshift estimate for any of the three bluer models (the elliptical galaxy is ruled out because of the large excess of flux that should be observed at infrared wavelengths).

The redshifted and absorbed spectrum of every galaxy model is then integrated with the throughputs of the HST and Kitt Peak filters (including instrumental throughputs, made available through the HST and Kitt Peak databases) in order to obtain the expected measured fluxes for every galaxy type and redshift.

## 4.2. Redshift likelihood functions

Once the expected fluxes in all seven bands are calculated for all the models, we construct the redshift likelihood functions according to the following scheme. Assuming that the flux uncertainties are normally distributed, the likelihood  $L(z, T)$  of obtaining measured fluxes  $f_i$  with uncertainties  $\sigma_i$  given modeled fluxes  $F_i(z, T)$  for a given spectral type  $T$  at redshift  $z$ , with a flux normalization  $A$  over the seven filters ( $i = 1 - 7$ ) is

$$L(z, T) = \prod_{i=1}^7 \exp \left\{ -\frac{1}{2} \left[ \frac{f_i - AF_i(z, T)}{\sigma_i} \right]^2 \right\}. \quad (8)$$

This likelihood function is then maximized with respect to spectral type and normalization  $A$  to obtain the redshift likelihood function  $L(z)$ . The redshift likelihood function is then maximized with respect to redshift to yield the maximum-likelihood estimate of the redshift,  $z_{\text{phot}}$ .

The likelihood functions  $L(z)$  should not only give estimates of  $z$ , but also some confidence level around the best-fit value. Unfortunately, the problem is not a well-defined one because of the cosmic variance involved in the selection of a finite—and in our case small—number of spectral templates. Because of this effect, we cannot in general define real confidence limits, but only use in an orientative way the likelihood functions to distinguish those cases where the value of  $z_{\text{phot}}$  is susceptible of error—e.g., those ones where the function  $L(z)$  is multi-modal. For the same reason, individual values of  $L(z)$  corresponding to the maximum  $z = z_{\text{phot}}$  are not good measurements of the goodness of fit. For example, they are completely dominated by the cosmic variance in

those cases where the sources are bright enough to make the photometric uncertainties very small, which renders very low values of  $L(z)$  even for apparently excellent fits. Nevertheless, as we will discuss in the next Section, photometric errors dominate over cosmic variance at magnitudes  $AB(8140) \gtrsim 26$ . In this regime the likelihood functions do handle the errors properly, so confidence limits on  $z$  can be obtained from them in the usual way.

## 5. The catalog

We present in this Section the last steps performed on the object list in order to reach the final catalog. These include the correction of those single objects that were broken into separate pieces by SExtract and the elimination of stellar objects in the HDF.

### 5.1. Correction of deblended objects

Automatic deblending of object images has been known for a long time to be a very difficult task. Although SExtract does a very good work in creating the initial list from the F814W image, a careful examination of the segmentation maps shows that some groups of very close images, that might well belong to the same physical object—however difficult this might be to define—have been broken into separate pieces in our catalog. We decide to attack this problem *after* the photometric analysis has been performed, because in this way we can use the color information—together with the redshift estimate—of each of the pieces in every group to decide whether or not to add them together into one single object.

We select from the catalog all those pairs (or larger groups) of objects whose centers lie on the image at distances smaller than 2 arc seconds—or 3 arc seconds if any of the objects has  $AB(814) < 24.0$ . These groups are analyzed in a one-by-one basis, and in those cases where the colors of the sub-clumps are found to be compatible and the images suggest that there is only one source, we add the corresponding fluxes together in an optimal way and repeat the calculation of the redshift likelihood for the resulting single object.

The total number of groups analyzed in this way was over 200, most of them pairs and also some triads and even larger groups. In approximately half of the cases the sub-objects were found to share similar colors, and hence were added together as a single entry in the catalog. This procedure makes our catalog less prone to the over-counting of faint small objects (see Colley *et al.* 1996) and the numbers involved show that it can indeed pose a problem at the high resolution achieved with HST imaging.

## 5.2. Stars in the HDF images

We have decided not to include a stellar spectrum in our set of SEDs in this work. We take this decision based on two facts. First, our previous analysis (LYF) did include a M star template and we found that none of the objects was better fitted by it than by any of the galaxy templates. Second, and most important, several compilations have been published of point-like sources in the HDF (Flynn, Gould & Bahcall 1996, Elson, Santiago & Gilmore 1996, Méndez *et al.* 1996, Cowie 1997). Using them we have chosen all the objects that appear as stellar at least in one of the references—20 objects in total, including an obvious star not included in them possibly because of its position being too close to the border of the images—, and subsequently eliminated them from our catalog. Table 3 lists the sources that have been eliminated.

## 5.3. The final catalog

The complete catalog contains 1067 entries. The inner area of the HDF images (Z1) contains 946 galaxies over an area of 3.92 arcmin<sup>2</sup>, reaching down to magnitude  $AB(8140) = 28.0$ . The outer area (Z2) is less deep, containing 121 objects with magnitudes down to  $AB(8140) = 26.0$  over an area of 1.39 arcmin<sup>2</sup>.

Table 4 lists the coordinates, *best*  $AB(8140)$  magnitudes, redshifts (both spectroscopic, if available, and photometric) and best-fit spectral types for every galaxy in the catalog, together with the corresponding ID in the Williams *et al.* (1996) catalog. Table 5 lists the *aperture* fluxes of every object in all seven  $UBVIJHK$  bands together with their associate  $1\sigma$  errors in nJy. The relations between  $AB$  magnitudes and flux are given by:

$$AB_{\lambda} = -2.5 \log f_{\nu}(\text{erg cm}^{-2}\text{s}^{-1}\text{Hz}^{-1}) - 48.60 = -2.5 \log f_{\nu}(\text{nJy}) + 31.40. \quad (9)$$

Tables 4 and 5 (both in HTML format) are available in the *on line* edition, and include links from every object entry to its individual data page. Both Tables, together with the catalog in electronic form and a clickable map to help with the object identification, are available upon request from the authors, and also at the following WWW address: <http://bat.phys.unsw.edu.au/~fsoto/hdfcat.html>.

## 6. Comparison with spectroscopic redshifts

As was mentioned before, there are  $\approx 100$  galaxies in the HDF that have had their redshifts already determined through spectroscopy (Cohen *et al.* 1996, Cowie 1997, Steidel *et al.* 1996, Zepf

*et al.* 1997, Lowenthal *et al.* 1997). As is explained in Lanzetta, Fernández-Soto and Yahil (1997), there have been problems regarding the identification of sources in the HDF that render some of the spectroscopic redshifts uncertain. After a very careful check procedure, we have obtained a list of reliable redshifts and enriched it with some data not yet published (kindly provided by Spinrad and Steidel and Dickinson, see also Dickinson *et al.* 1997).

This list contains 108 redshifts. The comparison between the photometric and spectroscopic values is shown in Figure 6. These are the main features that can be extracted from it:

1. There are two obvious errors corresponding to high-redshift 1. galaxies ( $z > 2$ ) to which we have assigned low-redshift values. Their numbers in the catalog are 687 ( $z_{\text{sp}} = 2.931$ ,  $z_{\text{phot}} = 0.280$ ) and 1044 ( $z_{\text{sp}} = 2.008$ ,  $z_{\text{phot}} = 0.040$ ). In both cases the redshift likelihood functions show secondary peaks close to the true value (3.120 and 2.280 respectively), but the SEDs are better fitted by the wrong redshift. We have made some attempts to change the model SEDs in order to avoid these problems, but any change in the templates that leads to the correction of this problem causes other fits to go wrong.

2. The rest of the high-redshift sample (27 objects, 93% of total galaxies with  $z > 2$ ) shows an acceptable distribution in the  $z_{\text{sp}} - z_{\text{phot}}$  plane, with an *rms* dispersion  $\Delta_{\text{rms}}z \approx 0.45$ . Over 70% of the total of objects (21 out of 29) have a deviation from the correct value which is less than 0.5 in redshift units. A general trend is noticed, however, to assign lower redshift values to the galaxies in the redshift range  $z = 2.0 - 2.5$ . We have tried but failed to find an explanation and a solution to this problem. It is not related to the absence of Lyman  $\alpha$  emission in our spectral templates, as there is no correlation between Lyman  $\alpha$  equivalent width and the measured value of ( $z_{\text{sp}} - z_{\text{phot}}$ ). Perhaps the inclusion of evolution in the models could palliate this problem somehow, at the price of including more parameters in the fit.

3. At low redshift ( $z < 1.50$ ) the situation is essentially perfect, with a dispersion  $\Delta_{\text{rms}}z = 0.13$ . If the 5 points with  $|z_{\text{sp}} - z_{\text{phot}}| > 0.20$ —which represent 6% of the sample—are eliminated, the dispersion goes down to  $\Delta_{\text{rms}}z = 0.09$ .

It is worth remarking that the scatter of the high redshift values is comparable to the one of the low redshift ones, if we use as estimator the value of  $\Delta_{\text{rms}}z/(1+z)$ , with  $\Delta z = z_{\text{sp}} - z_{\text{phot}}$ . This choice is justified by the functional dependence of most physical quantities on redshift. The values of this estimator—using average redshifts 0.75 (low-redshift) and 2.75 (high-redshift)—are then 0.07 and 0.12, respectively. In Figure 7 we show the average values of this estimator when the data are binned in redshift (groups of nine or ten objects per bin). The points mark the median value of  $z$  and  $\Delta z/(1+z)$  for every bin, with the horizontal error bars showing the width of the bin and the vertical ones marking the 25% and 75% percentiles in every bin. In order to create this plot we have ignored the two very large high-redshift errors on which we already commented.

## 6.1. Photometric Errors versus Cosmic Variance

Once the identification of objects is secure and the spectroscopic redshifts have been double-checked to avoid possible mistakes (see Lanzetta *et al.* 1997), two different effects may contribute to the residuals between the photometric and the spectroscopic redshifts. These are cosmic variance and photometric uncertainties.

Cosmic variance influences the results because we are using a finite set of spectral templates to fit an otherwise continuum spectral type space. The fact that our templates do not exactly fit all possible spectral energy distributions will produce an uncertainty in the fitted redshifts. This uncertainty might be very large if any galaxy spectrum came up to be extremely different from all of our models. As mentioned above, this has not been observed in the spectra of high-redshift galaxies reported to date.

On the other side, even for those galaxies whose spectral energy distribution would be perfectly fitted by one of our templates, the photometric uncertainties will produce a residual between real and estimated redshift. This residual is obviously expected to be increasingly important as a function of apparent magnitude.

In order to evaluate the relative importance of these two effects, we perform the test described here. First, we assume our photometric redshifts to be exact, and the best-fit models to be perfect fits to the unknown underlying galaxy spectra. In this way we get rid of the effect of cosmic variance, as all galaxies in our sample become exact copies of one of our four templates. Second, we add random noise (according to the actual flux uncertainties) to the best-fit model fluxes of all objects in all bands, and use these fluxes as input to our redshift-estimation program. All these steps are repeated 100 times, aiming to determine the distribution of residuals between the—supposedly— exact redshifts and the simulated ones. These residuals are now the *only* product of photometric uncertainties, as we have eliminated any cosmic variance by assuming that our best-fit model represent a perfect image of reality.

Figure 8 shows the distribution of residuals as a function of apparent magnitude (*best* total magnitudes are used throughout this Section) and redshift, together with the median residual for each bin. Several conclusions can be drawn from it:

1. Photometric error produces almost no effect on the photometric redshifts at magnitudes  $AB(8140) < 25$ , independently of redshift. At these magnitudes, the median absolute residual is no greater than 0.04, and the distributions of residuals are concentrated into single peaks centered at zero residual.

2. Photometric error produces a mild effect on the photometric redshifts at magnitudes  $AB(8140) = 25 - 26$ , somewhat more pronounced at redshifts  $z > 2$  than at redshifts  $z < 2$ . The median absolute residual (at all redshifts) is only 0.04 (comparable to the median absolute residual at brighter magnitudes), but the distributions of residuals at high-redshifts are spread into small secondary peaks centered at large negative residuals in addition to prominent primary peaks centered at zero residual. These secondary peaks result from high-redshift galaxies that are incorrectly assigned low redshifts and contain 2.5% of the total at redshifts  $z = 2 - 3$  and 6.1% of

the total at redshifts  $z = 3 - 4$ .

3. At magnitudes  $AB(8140) > 26$  photometric uncertainties produce an increasingly significant effect. At redshifts  $z = 0 - 1$ , the effect of photometric error at faint magnitudes is twofold: the median absolute residuals increase and long tails stretching to large positive residuals appear on the distributions. At redshifts  $z > 1$ , the effect of photometric error at faint magnitudes increases the median absolute residuals and produces prominent secondary peaks centered at large negative residuals on the distributions—the latter again due to the wrong assignment of low redshifts to high-redshift galaxies. In the magnitude range  $AB(8140) = 26 - 27$  these secondary peaks contain 9.7% of the total of objects at redshifts  $z = 2 - 3$  and 19.6% at redshifts  $z = 3 - 4$ .

4. At faint magnitudes, it is more likely that high-redshift galaxies will be incorrectly assigned low redshifts than that low-redshift galaxies will be incorrectly assigned high redshifts. For example, at magnitudes  $AB(8140) = 27 - 28$ , the long tail stretching to large positive residuals at redshifts  $z = 0 - 1$  contains 27.3% of the total while the secondary peak at large negative residuals at redshifts  $z = 3 - 4$  contains 34.8% of the total. This is also seen in the values of the median absolute residuals, that are 0.26 and 0.64, respectively.

We can combine these conclusions with the results of the previous subsection in order to assess the relative importance of cosmic variance and photometric uncertainties in the determination of photometric redshifts. The low-redshift sample that has been observed spectroscopically contains objects of magnitudes ranging from  $AB(8140) = 18.16$  to  $AB(8140) = 24.88$ , with a median of  $AB(8140) = 22.55$ . We have just shown that at these magnitudes photometric uncertainties produce no effect on the redshift estimates. The high-redshift galaxies with spectroscopic redshifts have magnitudes in the range  $AB(8140) = 23.24$  to  $26.75$ , with a median of  $AB(8140) = 24.75$ . In this range the effect of photometric uncertainties is—at most—mild. We conclude from this analysis that *residuals between the photometric and spectroscopic redshifts are dominated by cosmic variance rather than by photometric error*.

This important result establishes the magnitude of the effect of cosmic variance on the photometric redshifts. Specifically, we can attribute the entire residual between the photometric and spectroscopic redshifts to the effect of cosmic variance and consider the redshift range  $z \approx 0 - 4$  spanned by the comparison of photometric and spectroscopic redshifts and conclude that cosmic variance produces a median absolute residual of 0.08, a  $3\sigma$ -clipped *rms* residual of 0.18, and a discordant fraction of 0.057. If the effect of cosmic variance does not increase with decreasing galaxy luminosity—and we can think of no reason that it should—then these values must apply at all magnitudes, not just the relatively bright magnitudes of the spectroscopic limit.

This fact has two important implications: First, at magnitudes brighter than  $AB(8140) \approx 26 - 27$ , the accuracy and reliability of the photometric redshifts is limited by cosmic variance whereas at  $AB(8140) \geq 26 - 27$  it is limited by photometric error. Second, the uncertainty associated with any statistical moment of the galaxy distribution (including the effects of sampling error, photometric error, and cosmic variance) can be realistically estimated by



means of a bootstrap resampling technique, where the effect of photometric error is simulated by adding random noise to the fluxes and the effect of cosmic variance is mimicked by adding (rather modest) random noise to the estimated redshifts. We expect that this technique will ultimately play an important role in exploiting the full potential of the broad-band photometric redshift techniques.

## 7. Discussion

We want to discuss in this Section some of the most interesting properties of the distribution of galaxies in the HDF as revealed by our catalog. A more in-depth analysis is left for other papers (Lanzetta, Yahil & Fernández-Soto 1998, on the feasible presence of galaxies at  $z > 6$  detected only in the infrared images; Driver *et al.* 1998, on the combination of our catalog with galaxy morphological information; Lanzetta, Fernández-Soto & Yahil 1998, on the highest-redshift candidates in the HDF; Pascarelle, Lanzetta & Fernández-Soto 1998, on the measurements of the Star Formation History of the universe; and Fernández-Soto, Lanzetta & Yahil 1998, on the Luminosity Functions as measured from the catalog). We will only introduce in this Section some of the basic properties of the galaxy distribution.

### 7.1. Number counts

Figure 9 shows the  $I$ -band number counts as measured from our catalog, corrected for the different sizes of the zones Z1 and Z2. On the same diagram we show the results from some previous studies. The number counts agree in the common magnitude range, and it is clear from this plot the extension that the HDF images represent for this kind of studies. It must be noted, however, that the points representing the work of Driver *et al.* (1995) correspond only to total counts for their morphologically classified sample, with the number counts for unclassified objects reaching deeper. In any case, because of the small size and the particular characteristics of the field that was chosen for the HDF, it cannot be expected to represent the general galaxy population, specially at the bright end. Driver *et al.* (1998) provide a more in-depth study of these data combining the redshift information with the morphological classification obtained by using an Artificial Neural Network.

We can also use the infrared images to measure number counts down to magnitudes  $J = 23.5$ ,  $H = 22.5$ , and  $K = 22.0$ . Although our sample has been selected in the  $I$ -band, we can define complete samples in the infrared given the fact that the  $I$ -band image is much deeper than any of the others. This has been checked via an analysis of the residual infrared images, where only one object brighter than the limits given above was found (in the  $K$ -band image, see Lanzetta *et*

*al.* 1998). Figure 10 shows these number counts. We have used in this case standard magnitudes instead of the  $AB$  system in order to make the comparison with other published works easier.

## 7.2. The redshift distribution

Figure 11 shows the redshift distribution of the galaxies in our catalog. We have divided the sample in two different magnitude bins (objects with  $AB(8140) < 26.0$  and  $26.0 < AB(8140) < 28.0$ ) in order to show the change of the redshift distribution with magnitude. The median redshift for the bright magnitude bin is  $z_{\text{med}} = 1.00$ , and for the fainter one is  $z_{\text{med}} = 1.56$ .

A more detailed analysis of the redshift-magnitude distribution is given in Figures 12 and 13. The first one shows the change of the median redshift as a function of apparent magnitude limit while the second one shows the cumulative (and doubly cumulative) distribution of redshift for different magnitude-limited samples. Both figures show clearly that the median redshift increases as a function of the apparent magnitude limit only up to  $AB(8140) \approx 26$ , remaining approximately constant for fainter magnitudes.

## 7.3. Hubble Diagram

Having photometric measurements in seven bands and estimated redshifts, we can calculate an estimate of the absolute magnitude of every object in the catalog without the need to use K-corrections. The Hubble Diagram is a simple although powerful way to show the data and to analyze them. Of course a more detailed analysis requires a careful calculation of the Luminosity Function, together with a proper estimation of the errors implied in its determination. Nevertheless, and for the sake of completeness, we show in Figure 14 the rest-frame  $U$ -band absolute magnitude of the objects in our sample as a function of redshift. We have separated them according to the rough spectral classification given by the best-fit spectrum to each object. The choice of  $U$ -band magnitudes is given by the fact that we are calculating rest-frame magnitudes from our best-fit spectra, and the use of a shorter wavelength allows for the corresponding observed band to remain in the optical part of the spectrum for a larger redshift range—up to  $z \approx 2$  in the case of the  $U$  band, only  $z \approx 1$  for the  $B$  band. The very large excess of Irregular galaxies at high redshifts might not be completely real because, as was mentioned before, at redshifts  $z > 3$  most objects are only seen in—at most—the two reddest HST bands and are too faint to be securely detected in the IR images. In this case the only observable feature is the position of the Lyman Limit, which is obviously insufficient to provide a good estimate of the spectral type. Our algorithm tends in this situation to choose the Irregular SED as the best fit simply because of the

relatively smaller flux it provides in the redder filters—which better fits the data in every case. Nevertheless, once this has been remarked, we should note that the morphological classification of galaxies in the HDF with  $AB(8140) < 26.0$  as provided in Odewahn *et al.* (1996) and studied in conjunction with this catalog in Driver *et al.* (1998) shows that there is a real excess of this class of objects at redshifts larger than  $z = 1.5$ , together with a lack of disk galaxies over the same redshift range.

#### 7.4. High-redshift candidates

An important result from the LYF paper was the detection of galaxies in the HDF with estimated redshifts as high as  $z \approx 6$ . One of those candidates (object #213 in our catalog,  $z_{\text{phot}} = 5.64$ ) has already been spectroscopically confirmed (Weymann *et al.* 1998,  $z_{\text{sp}} = 5.60$ ), and the infrared observations described in Section 2 support the high-redshift hypothesis for most of them (for more details, see Lanzetta, Fernández-Soto & Yahil 1998).

First, none of the candidates shows up as a strong infrared emitter. In case the breaks observed in the flux of these objects between the  $V$  and  $I$  bands were due to very strong reddening by dust, as has been suggested, the spectral energy distributions should rise very steeply towards the infrared—implying very red ( $I - K$ ) colors, which is not observed.

Second, the HST images alone allowed for the interpretation of those candidates as objects in which a single extremely strong emission line is contributing all the flux seen in the  $I$  band, with the continuum being too weak to be detectable in all  $U$ ,  $B$ , and  $V$  bands. This possibility is discarded by the fact that several of the candidates are detected in at least one of the infrared bands.

Table 6 shows the data for the six high-redshift brightest candidates in our catalog. All of them have magnitudes  $25 < AB(8140) < 26.5$ , which puts them at the very limit of feasible spectroscopic confirmation with either Keck LRIS or STIS on board HST. Object E has been observed by Spinrad using the Keck telescope in Hawaii, and has been *tentatively* assigned a redshift of  $z = 4.58$  (Spinrad 1997). Figure 15 shows the  $UBVIJHK$  images for all six objects, with the spectral energy distributions and redshift likelihood functions shown in Figure 16. From them it can be seen that the spectral energy distributions of objects C, D, and F can also be fitted with a low-redshift solution. Though in all cases the goodness of fit is better for the high-redshift case, we consider that objects A, B and E are the ones for which the evidence favoring the high-redshift hypothesis is stronger. The Weymann *et al.* (1998) object is even fainter than these, and is hence not included in this list.

Object A is particularly interesting because of its brightness ( $AB(8140) = 25.69$ ) and its morphology. It has the same colors—to within photometric errors—as the fainter object to its left, which has  $AB(8140) = 26.52$ . In fact, if they are taken together as a single object in the same

way described in Section 5, their joint magnitude is  $AB(8140) = 25.30$  and the best-fit redshift is 5.28. The reason why both objects have not been added together in the catalog is that they lie in the outer zone (Z2), hence the faint one is too faint to appear in the main catalog. The angular distance separating both clumps is 0.5 arc seconds, which corresponds to  $1.5 h_{100}^{-1}$  kpc for  $q_0 = 0.5$ . After this paper had been submitted Spinrad *et al.* (1998) succeeded in measuring the redshift of this faint double galaxy, finding a value  $z_{\text{sp}} = 5.34 \pm 0.01$ , in excellent agreement with the above mentioned photometric redshift.

## 8. Conclusions

We have presented the results of a detailed 7-band photometric study of the Hubble Deep Field together with a catalog of estimated redshifts. The final catalog contains 1067 objects, is free of stellar and point-like objects and is complete down to magnitude  $AB(8140) = 28.0$  in the inner  $3.93 \text{ arcmin}^2$  of the HDF images and down to  $AB(8140) = 26.0$  over the whole field.

One of the main steps taken to build this catalog is the accurate photometry of the IR images provided by Dickinson *et al.* (1998). We have developed an optimal method to measure the IR fluxes of all objects detected in the HST images which doesn't rely on their detection in the IR images, which allows for the measurement of faint fluxes in very small objects.

We have tested the quality of the redshift estimates by comparing our results with a list of 106 spectroscopically determined redshifts from the literature. The agreement is essentially perfect in the low-redshift regime ( $z < 1.5$ ), with a  $\Delta z_{\text{rms}}$  dispersion of 0.13 and only 6% of the objects having a difference between photometric and spectroscopic redshift larger than 0.20. At high redshift ( $z > 2.0$ ) the situation is somehow worse. Our method underestimates the values in the redshift range  $z = 2.0 - 2.5$  by an average  $\Delta z = 0.45$ . We have a catastrophic error (i.e.,  $\Delta z > 1.5$ ) rate of 7% (2 out of 27) in this range. Ignoring these two outliers, the average dispersion is  $\Delta z_{\text{rms}} = 0.45$ , with more than 70% of the objects having their redshift determined to an accuracy of  $\Delta z = 0.50$  or better. The average dispersion is significantly smaller if the systematic trend observed in the redshift range  $z = 2.0 - 2.5$  mentioned before is taken into account.

We have tested the relative importance of photometric errors and cosmic variance in producing the observed dispersion of measurements. Our calculations show that cosmic variance (i.e., the fact that our set of models is only a finite sample of all possible galaxy spectra) is the only source of error for objects with apparent magnitudes down to  $AB(8140) < 25.0$ . Photometric errors start to be important in the magnitude range  $25.0 < AB(8140) < 26.0$ , specially for objects at  $z > 2.0$ . The photometric errors alone can account for up to 3 – 6% erroneous redshift estimates in that range. These numbers become as large as 10 – 20% for  $26.0 < AB(8140) < 27.0$  and 25 – 35% for  $27.0 < AB(8140) < 28.0$  (where the figures represent the catastrophic error rate in the redshift intervals  $z = 2.0 - 3.0$  and  $3.0 - 4.0$  respectively).

The important point that can be deduced from this analysis is that at the magnitudes span by the available spectroscopic redshifts cosmic variance is the only important source of error. Hence we can estimate the importance of cosmic variance from our comparison. We obtain that it produces—over the complete redshift range  $z = 0.0 - 4.0$ —a median error of  $\Delta z_{\text{med}} \approx 0.08$ , a dispersion of  $\Delta z_{\text{rms}} \approx 0.18$  and a discordant rate of 0.057. These numbers will be important to assess the systematic error bars in any future analyses to be performed using this catalog.

We have finished our work by sketching some of the basic statistical properties of the ensemble of galaxies in the HDF and showing a selection of  $z \approx 5$  candidate objects. These galaxies as well as the whole catalog are already the subject of subsequent studies.

We would like to thank Bob Williams and the entire STScI HDF team for providing the astronomical community with such an exciting image as the HDF is. We also thank John Webb for allowing us to use his data on the Lyman  $\alpha$  decrement, Mark Dickinson for making the IR images available and Hy Spinrad, Chuck Steidel, and once again Mark Dickinson for allowing us to use some of their spectroscopic observations prior to their publication. We particularly acknowledge the comments from our referee Rogier Windhorst, that have been very valuable in improving the clarity of the paper. A.F.S. acknowledges support from a grant from the Australian Research Council. A.F.S. and K.M.L. were supported by NASA grant NAGW-4422 and NSF grant AST-9624216. This research has made extensive use of NASA’s Astrophysics Data System Abstract Service and the Los Alamos National Laboratory Astrophysics e-print Archives.

## REFERENCES

- Bertin, E., & Arnouts, S. 1996, A&AS, 117, 393
- Bruzual, G., & Charlot, S. 1993, ApJ, 378, 47
- Casertano, S., Ratnatunga, K. U., Griffiths, R. E., Im, M., Neuschaefer, L. W., Ostrander, E. J., & Windhorst, R. A. 1995, ApJ, 453, 599
- Cohen, J. G., Cowie, L. L., Hogg, D. W., Songaila, A., Blandford, R., Hu, E. M., & Shopbell, P. 1996, ApJ, 471, L5
- Coleman, G. D., Wu, C. C., & Weedman, D. W. 1980, ApJS, 43, 393
- Colley, W. N., Rhoads, J. E., Ostriker, J. P., & Spergel, D. N. 1996, ApJ, 473, L63
- Connolly, A. J., Csabai, I., Szalay, A. S., Koo, D. C., Kron, R. G., & Munn, J. A. 1995, AJ, 110, 2655
- Cowie, L. L. 1997, <http://www.ifa.hawaii.edu/~cowie/tts/tts.html>
- de Jong, R. S., & van der Kruit, P. C. 1994, A&AS, 106, 451
- de Jong, R. S. 1996, A&A, 313, 45
- Dickinson, M., 1997, in The Hubble Deep Field, proceedings of the Space Telescope Science Institute 1997 May Symposium, eds. M. Livio, S. M. Fall, and P. Madau, in press (also /astro-ph/9802064)
- Dickinson, M., *et al.* 1998, in preparation
- Driver, S. P., Fernández-Soto, A., Couch, W. J., Odewahn, S. C., Windhorst, R. A., Phillipps, S., Lanzetta, K. M., & Yahil, A. 1998, ApJ, 496, L93
- Driver, S. P., Windhorst, R. A., & Griffiths, R. E. 1995, ApJ, 453, 48
- Driver, S. P., Windhorst, R. A., Ostrander, E. J., Keel, W. C., Griffiths, R. E., & Ratnatunga, K. U. 1995, ApJ, 449, L23
- Elson, R. A. W., Santiago, B. X., & Gilmore, G. F. 1996, NewA, 1996, 1, 1
- Fernández-Soto, A., Lanzetta, K. M., & Yahil, A. 1998, in preparation
- Flynn, C., Gould, A., & Bahcall, J. N. 1996, ApJ, 466, L55
- Hogg, D. W., *et al.* 1998, AJ, 115, 1418
- Kinney, A. L., Bohlin, R. C., Calzetti, D., Panagia, N., & Wyse, R. F. G. 1993, ApJS, 86, 5
- Krist, J. 1995, in Astronomical Data Analysis Software and Systems IV, ASP Conference Series, 77, eds. R.A. Shaw, H.H. Payne, & J.J.E. Hayes, p. 349
- Lanzetta, K. M., Fernández-Soto, A., & Yahil, A. 1997, in The Hubble Deep Field, proceedings of the Space Telescope Science Institute 1997 May Symposium, eds. M. Livio, S. M. Fall, and P. Madau, in press (also /astro-ph/9709166)

- Lanzetta, K. M., Fernández-Soto, A., & Yahil, A. 1998, ApJ, submitted
- Lanzetta, K. M., Yahil, A., & Fernández-Soto, A. 1996, Nature, 381, 759
- Lanzetta, K. M., Yahil, A., & Fernández-Soto, A. 1998, AJ, in press (also /astro-ph/9806226)
- Leitherer, C., Ferguson, H. C., Heckman, T. M., & Lowenthal, J. D. 1995, ApJ, 454, L19
- Loh, E. D., & Spillar, E. J. 1986, ApJ, 303, L154
- Lowenthal, J. D., Koo, D. C., Guzmán, R., Gallego, J., Phillips, A. C., Faber, S. M., Vogt, N. P., Illingworth, G. D., & Gronwall, C. 1997, ApJ, 481, 673
- Madau, P. 1995, ApJ, 441, 18
- Méndez, R. A., Minniti, D., DeMarchi, G., Baker, A., & Couch, W. J. 1996, MNRAS, 283, 666
- Odewahn, S. C., Windhorst, R. A., Keel, W. C., & Driver, S. P. 1996, ApJ, 472, L13
- Pascarelle, S. M., Lanzetta, K. M., & Fernández-Soto, A., 1998, ApJ, submitted
- Pozzetti, L., Bruzual, A. G., & Zamorani, G. 1996, MNRAS, 281, 953
- Spinrad, H. 1997, private communication
- Spinrad, H., Stern, D., Bunker, A., Dey, A., Lanzetta, K. M., Yahil, A., Pascarelle, S. M., & Fernández-Soto, A. 1998, AJ, submitted
- Steidel, C. C., Giavalisco, M., Dickinson, M., & Adelberger, K. 1996, AJ, 112, 352
- Webb, J. K., 1996, private communication
- Weymann, R. J., Stern, D., Bunker, A., Spinrad, H., Chaffee, F. H., Thompson, R. I., & Storrie-Lombardi, L. J. 1998, ApJ, in press (also /astro-ph/9807208)
- Williams, R. E., et al. 1996, AJ, 112, 1335
- Zepf, S. E., Moustakas, L. A., & Davis, M. 1997, ApJ, 474, L1

Fig. 1.— The zones Z1 and Z2 in the WFPC2 images. The outer dotted line marks the borders of the  $4096^2$  mosaic image. The continuous line is the area in the mosaic covered by the WFPC2 field, and the inner dashed line separates the inner Z1 and outer Z2 zones.

Fig. 2.— Comparison of the different bands and model images. The panels correspond to a region of  $48 \times 48 \text{ arcsec}^2$  in chip 4. The upper panels show the F814W and  $K$ -band images. The lower left panel is the  $K$ -band model image as described on the text. The lower right corner shows the image resulting from subtracting the model from the original  $K$ -band image.

Fig. 3.— Distribution of values of the parameter  $q$  in all IR bands. From left to right the distributions correspond to the  $J$ ,  $H$ , and  $K$  band images. The superposed continuous lines are Gaussians with zero mean value and unit sigma, fitted to have the same number of objects as each of the distributions in the negative part. Observe the broadening of the positive tails of the distribution due to low-flux real objects.

Fig. 4.— Analysis of the residuals after model subtraction. The dotted lines show the distribution of pixel intensities in the areas of every image that do not correspond to any object ( $1\text{-}\sigma$  criterium). The continuous lines show the same distribution for the pixels that lie within objects. The distributions are very different in the original images (upper panels), but do agree sensibly once the model image is subtracted from the original (lower panels), showing the goodness of the fitting procedure. Note that the dotted lines (background) are the same in the upper and lower panels.

Fig. 5.— Spectral Energy Distributions used for the redshift estimation procedure. The models starting from the lowest one correspond to E/S0, Sbc, Scd, and Irr galaxies.

Fig. 6.— Comparison of photometric and spectroscopic redshifts.

Fig. 7.— Comparison of photometric and spectroscopic redshifts. The objects have been binned in groups of nine or ten per bin. The points correspond to the median redshift and value of  $\Delta z/(1+z) = (z_{\text{sp}} - z_{\text{phot}})/(1+z)$  per bin, with the horizontal error bars showing the width of the bin and the vertical error bars showing the 25% and 75% percentiles in each bin.

Fig. 8.— Effect of the photometric errors in the redshift determination procedure. Each box shows the result of the simulations for a given redshift and magnitude interval as labeled, together with the median redshift difference obtained. The graphic shows how the influence of the photometry becomes more important at fainter magnitudes, with both the median difference and the secondary peaks centered at the wrong redshift each becoming larger.



Fig. 9.— Galaxy number counts. The filled symbols correspond to our catalog of the HDF images. The empty circles show the results of Casertano *et al.* (1995), the empty squares those of Driver, Windhorst & Griffiths (1995), and the empty triangles those of Driver *et al.* (1995). The latter are only plotted to the magnitude at which the authors could morphologically classify the objects from their images ( $I < 24.5$ ).

Fig. 10.— Galaxy number counts in the  $J$ ,  $H$ , and  $K$ -bands. For clarity the counts in  $J$  and  $H$  have been displaced up two and one orders of magnitude respectively. The vertical lines mark the position of the  $5\sigma$  completeness limits. No completeness correction has been applied below these levels.

Fig. 11.— Galaxy redshift distribution from our catalog. We have broken the catalog in two magnitude-divided subsamples in order to show the change in the redshift distribution with magnitude.

Fig. 12.— Median redshift as a function of magnitude limit. For every magnitude bin, the filled triangle and the dashed line mark the median redshift and 68% interval around it for all galaxies within that redshift bin. The filled circle with the continuous line mark the same for the sample of galaxies with a magnitude flux in that bin or brighter. The positions of the different points and lines have been slightly offsetted for clarity.

Fig. 13.— Upper panel: Cumulative redshift distribution of galaxies in different magnitude bins. Each line shows the percentage of the galaxies within the magnitude range  $(m - 1, m)$ —starting at  $m = 22$  and moving towards the right to  $m = 28$ — that have redshift below a given value. Lower panel: Same but applied to the sample of galaxies with magnitude brighter than  $m$ . In both cases the lines alternate continuous and dotted style for clarity and the ticks close to the X-axis mark the median redshift for each of the magnitude-limited samples.

Fig. 14.— The Hubble diagram for the galaxies in our catalog. Each of the panels shows the diagram for each of the galaxy types assigned by our method. The dotted lines mark the detection limits set on the HDF images ( $18.0 < AB(8140) < 28.0$ ) taking into account the SED of every galactic type.

Fig. 15.—  $UBVIJHK$  band images of our six brightest high-redshift candidates. Each box is  $5'' \times 5''$  in size.

Fig. 16.— Spectral energy distributions and redshift likelihood functions for our six brightest high-redshift candidates. The solid dots mark the photometric data, while the open circles show the expected response from the best-fit model galaxy templates. Vertical error bars correspond to photometric errors and horizontal error bars indicate the FWHM of the filters.

Table 1: Parameters for the quadratic fit of the point spread function FWHM in every band ( $\text{FWHM}_{\text{pixels}} = a + br^2$ , where  $r$  = distance to the center of the image in pixels).

Band	$a$	$b$
$J$	6.4009	$3.454 \times 10^{-6}$
$H$	6.2030	$4.498 \times 10^{-6}$
$K$	6.1367	$3.722 \times 10^{-6}$

Table 2: Ages, types of Initial Mass Function and Star Formation Rates used by the Bruzual & Charlot (1993) code to generate the IR part of the model galaxy spectra. In the last column  $\tau_n$  denotes an exponentially decaying SFR with characteristic time of  $n$  Gyr.

Type	Age (Gyr)	IMF	SFR
E/S0	12.7	Scalo	$\tau_1$
Sab/Sbc	12.7	Scalo	$\tau_8$
Scd	12.7	Salpeter	Constant
Irr	0.1	Salpeter	Constant

Table 3: Stars in the Hubble Deep Field. The coordinates refer to  $(x, y)$  positions in the Mosaic images.

Coordinates		AB(8140)	References <sup>a</sup>
1877	349	23.52	1,2
3380	404	22.68	1,2
1306	420	24.64	1,2,4
869	988	19.22	1,4
247	1117	22.50	1,2,3,4
2904	1130	21.08	1,4
1194	1254	22.71	1,2,3,4
2449	1574	22.40	1,2,3,4
2070	1756	20.89	1
1026	1802	21.23	1,2,3,4
3425	1920	24.14	1,2,3,4
2441	1936	24.34	1,2,3,4
654	2180	19.26	1,4
1645	2496	27.61	3
535	2775	26.76	1,2,3
956	2845	25.42	1,2,3
1095	3203	26.38	1,2
315	3788	20.84	1,3
1389	3819	25.50	3
1361	3974	19.90	–

<sup>a</sup>The references are: 1) Flynn, Gould & Bahcall (1996), 2) Elson, Santiago & Gilmore (1996), 3) Méndez *et al.* (1996), 4) Cowie (1997). The last entry is an obvious star not present in any of the references, perhaps because it lies too close to the upper border of the image.

Table 6: Data corresponding to the brightest high-redshift candidates in our catalog.

Name	No <sup>a</sup>	Coordinates <sup>b</sup>				$z_{\text{phot}}$	$AB(8140)$
A	3	542.8	229.2	12:36:59.797	62:12:18.67	5.72 <sup>c</sup>	25.69
B	311	2342.2	968.4	12:36:48.714	62:12:16.72	5.64	26.32
C	328	2393.8	1006.4	12:36:48.357	62:12:17.28	4.76	26.19
D	868	407.6	2752.9	12:36:54.714	62:13:52.85	4.72	25.97
E	173	3259.2	652.1	12:36:44.658	62:11:50.45	4.58 <sup>d</sup>	25.04
F	479	887.0	1392.1	12:36:55.334	62:12:55.54	4.56	25.24

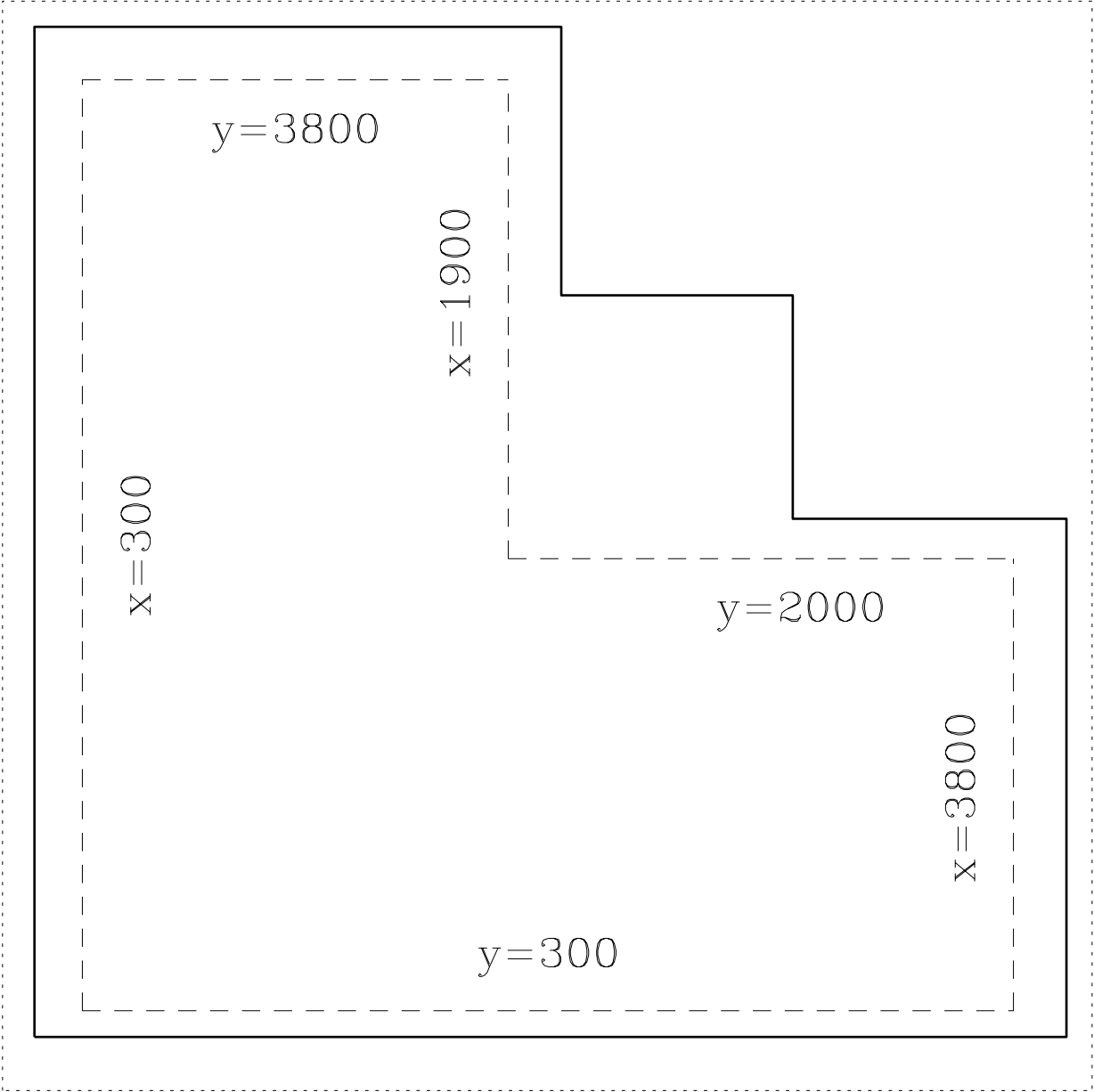
---

<sup>a</sup>Number in our catalog

<sup>b</sup>( $X, Y$ ) in the mosaic images and (RA, DEC)

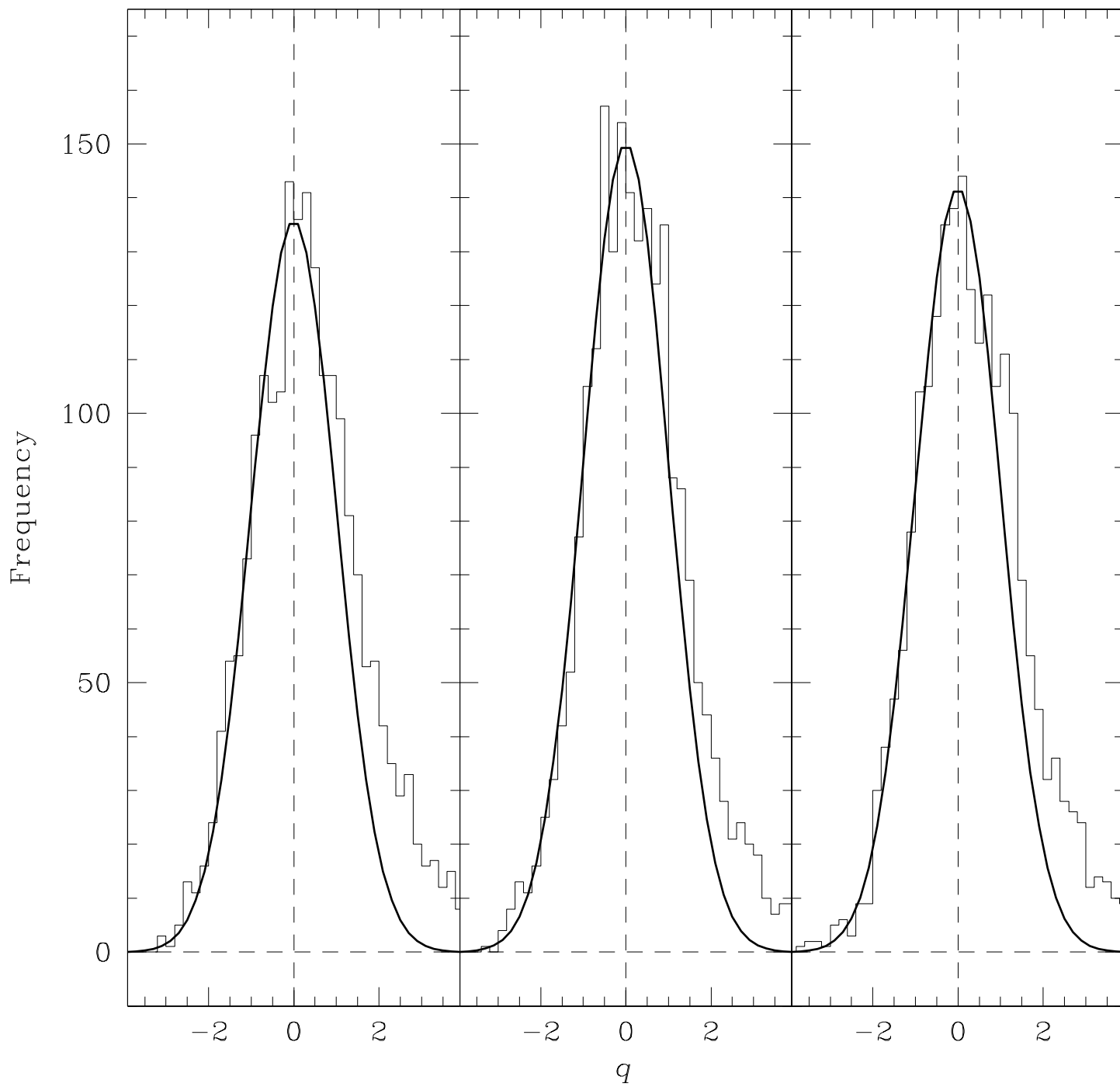
<sup>c</sup>Or  $z_{\text{phot}} = 5.28$ , see text for explanation.  $z_{\text{spec}} = 5.35$

<sup>d</sup>Tentative spectroscopic redshift (see text),  $z_{\text{phot}} = 4.52$

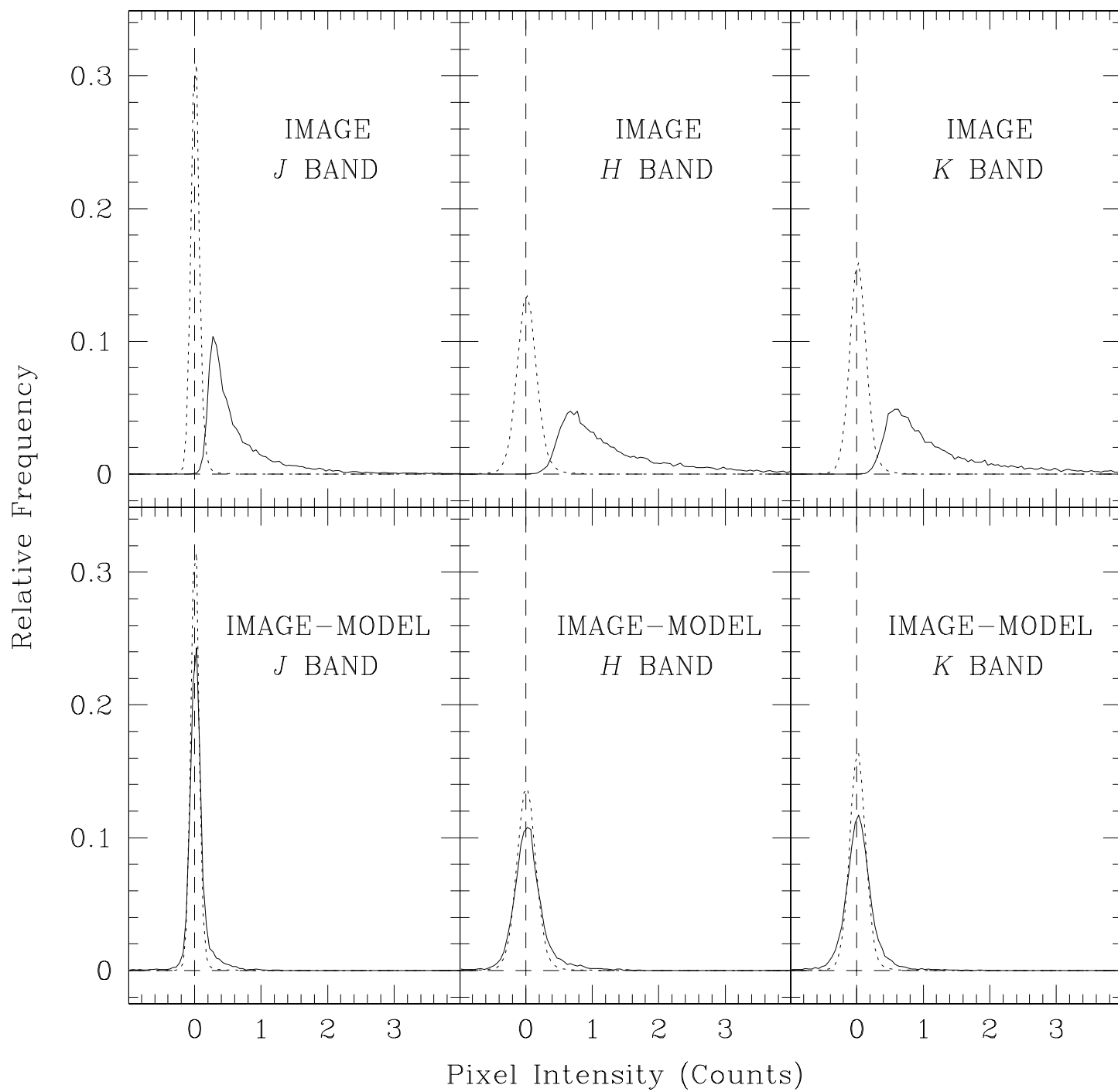


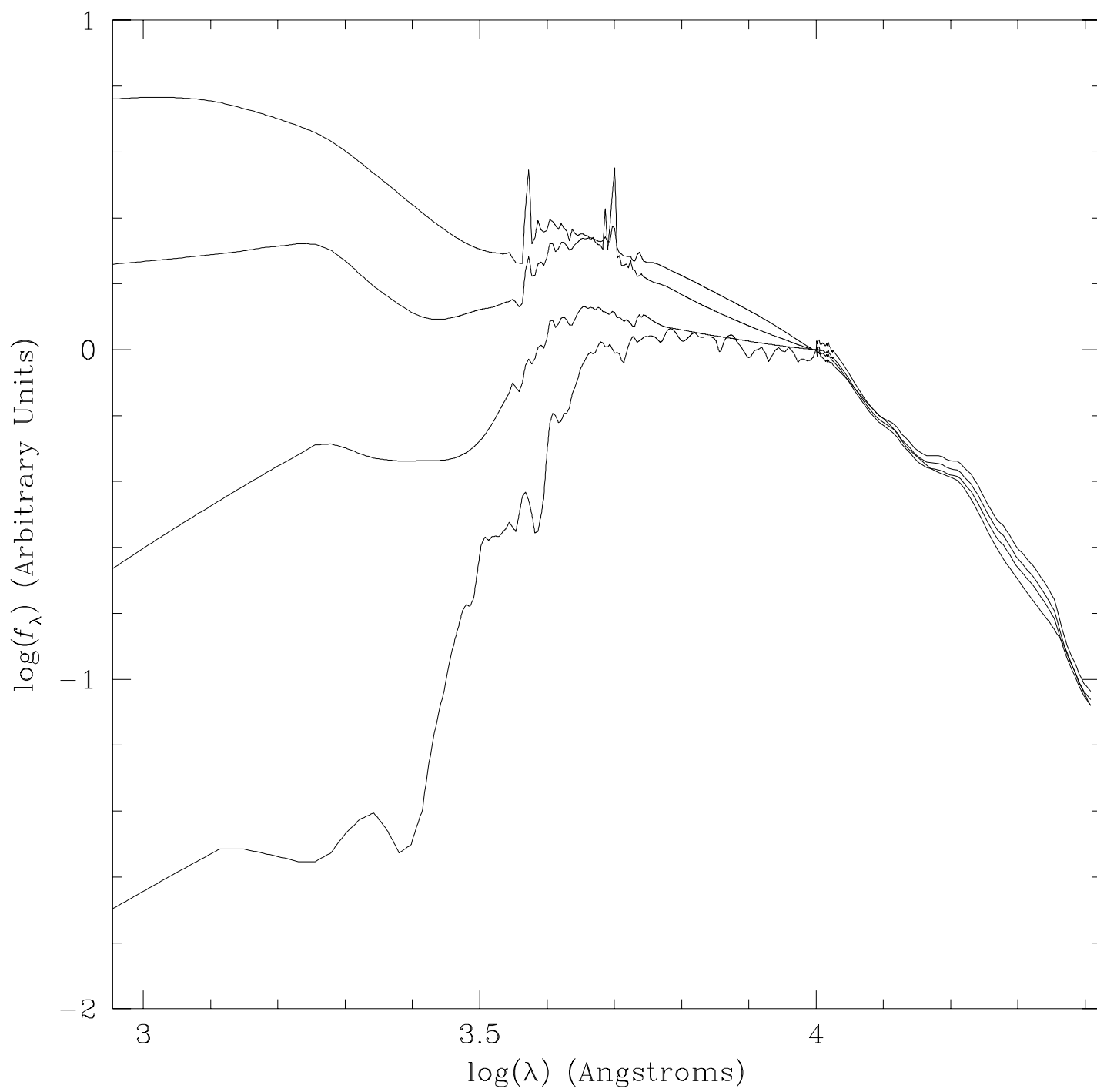
This figure "f2.jpg" is available in "jpg" format from:

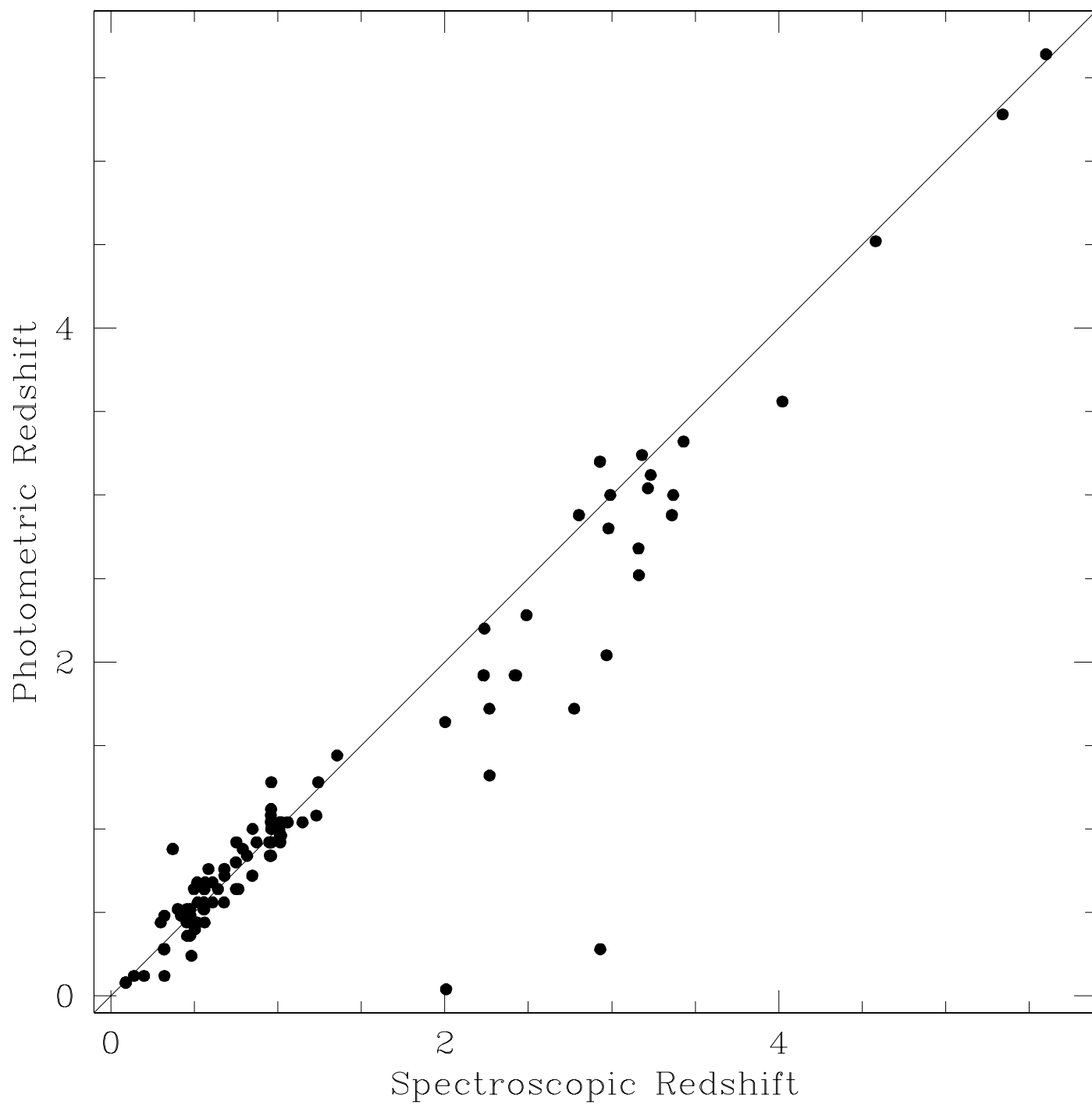
<http://arxiv.org/ps/astro-ph/9809126v1>

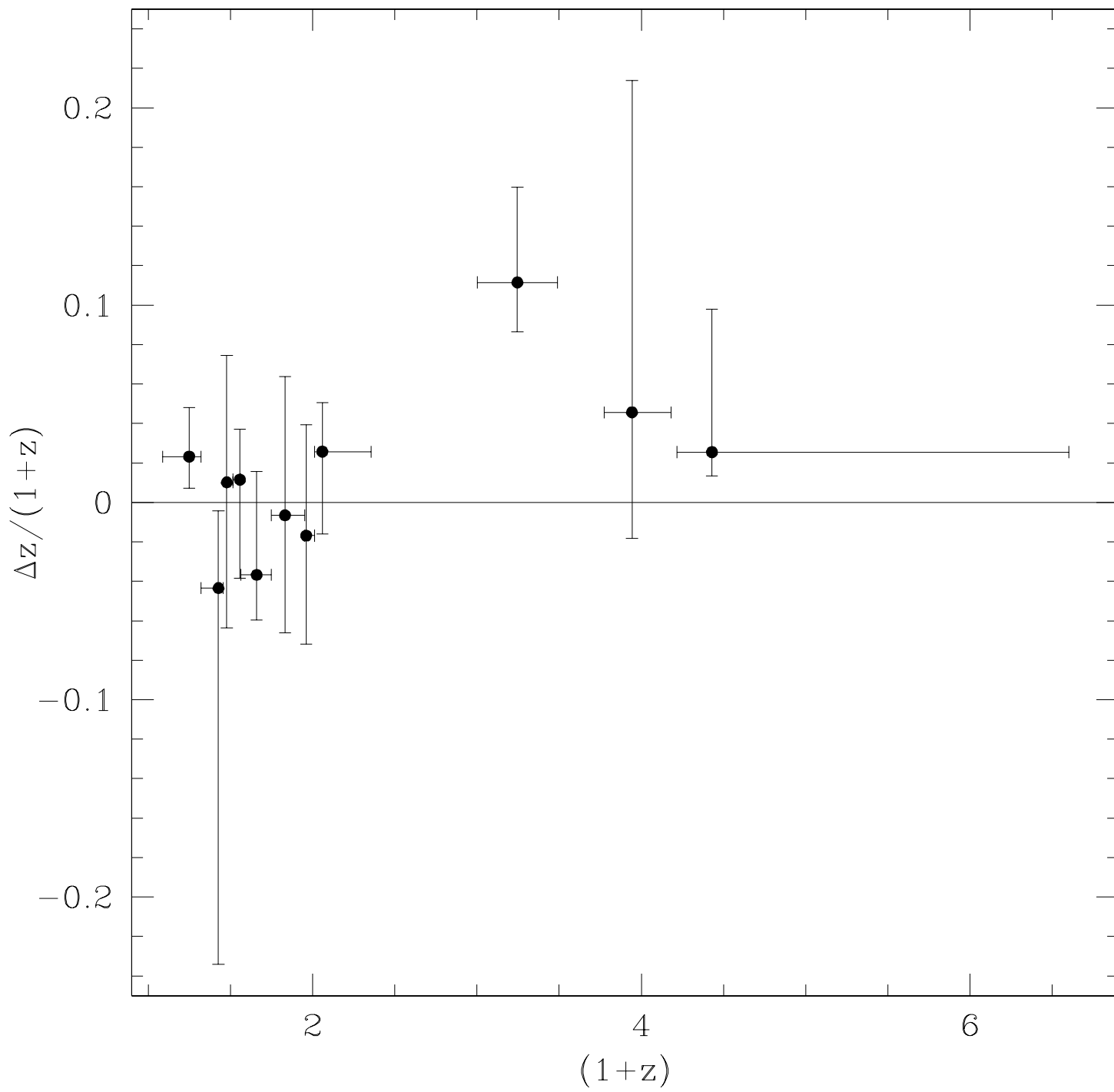






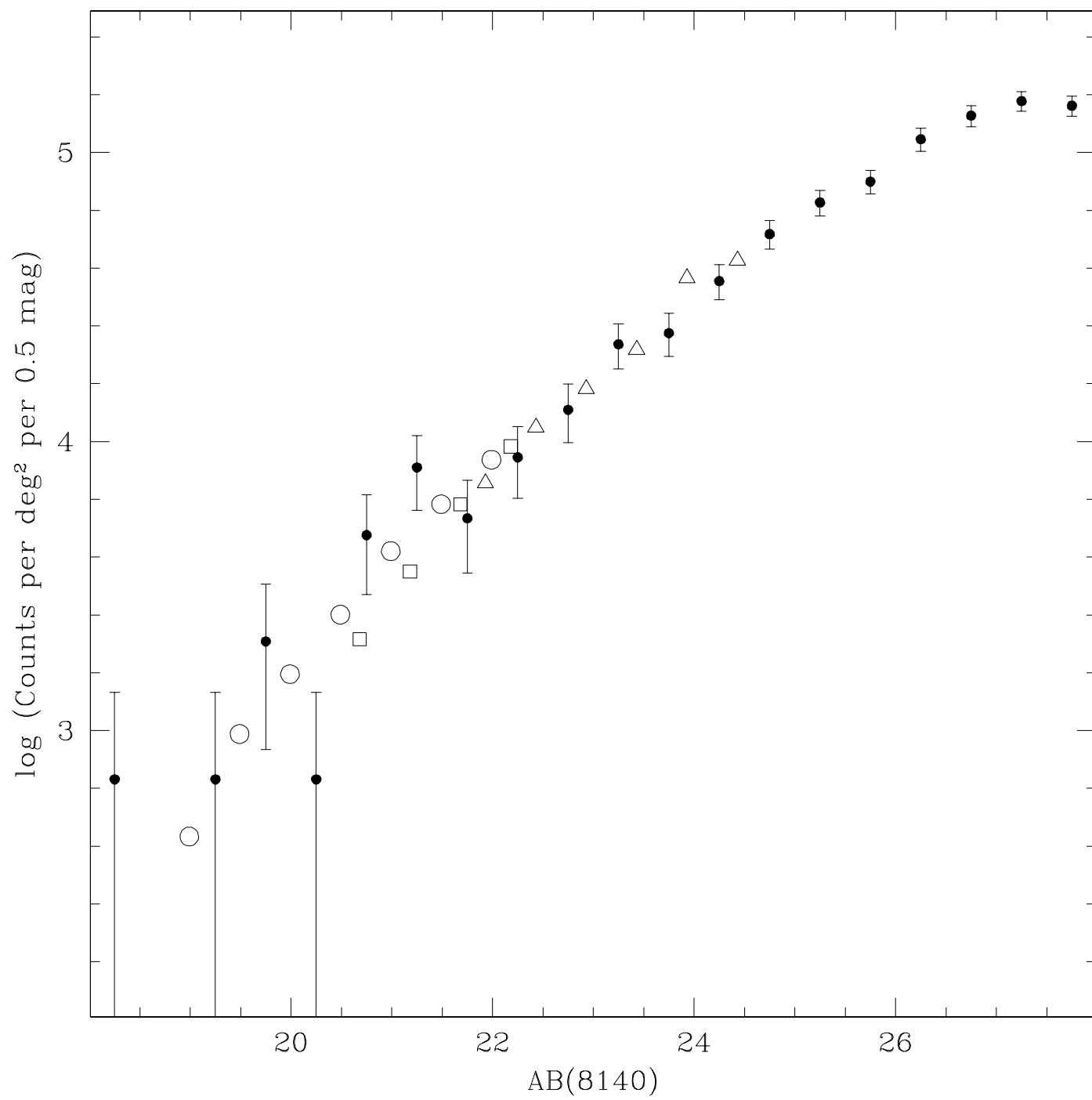


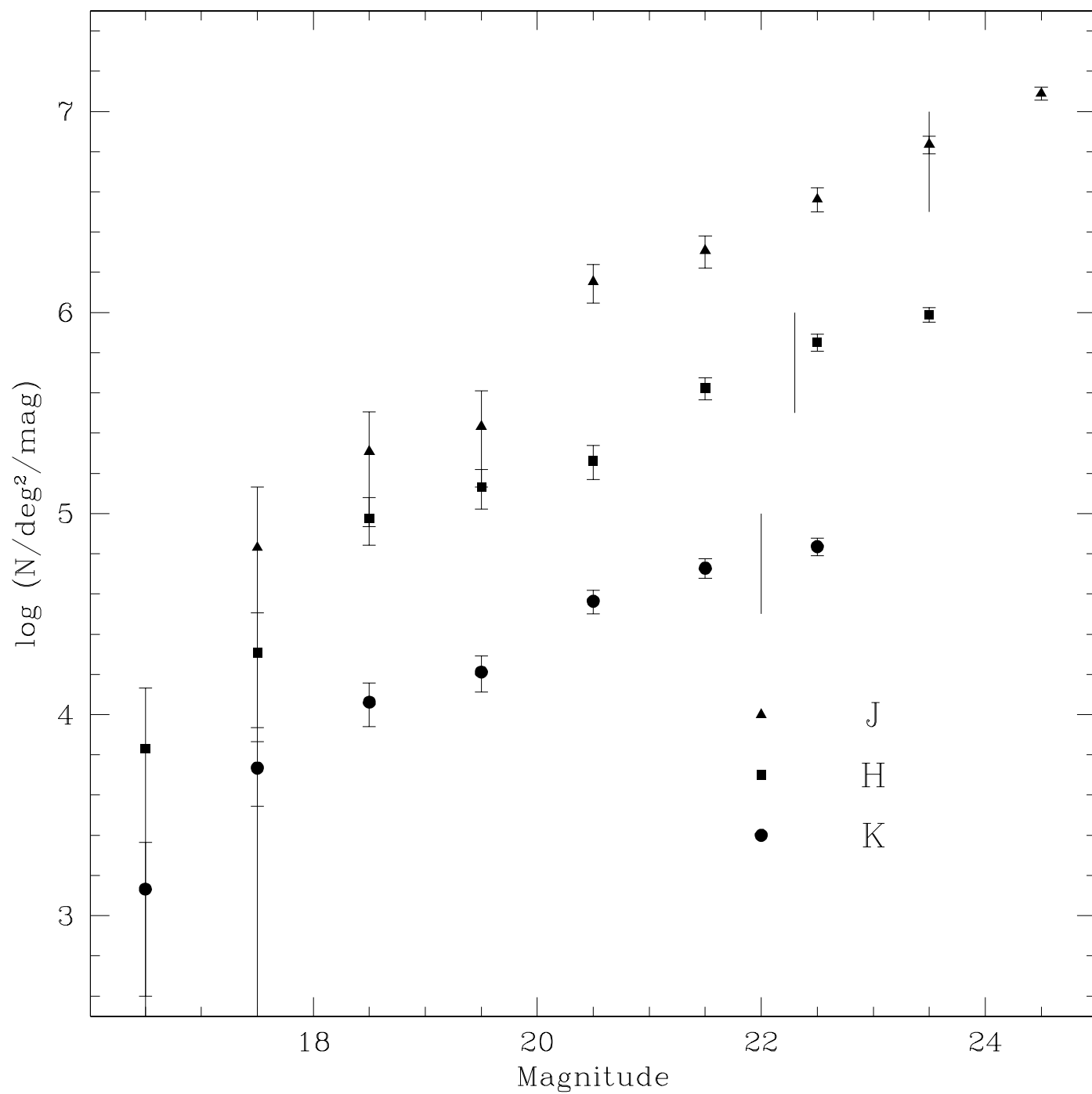


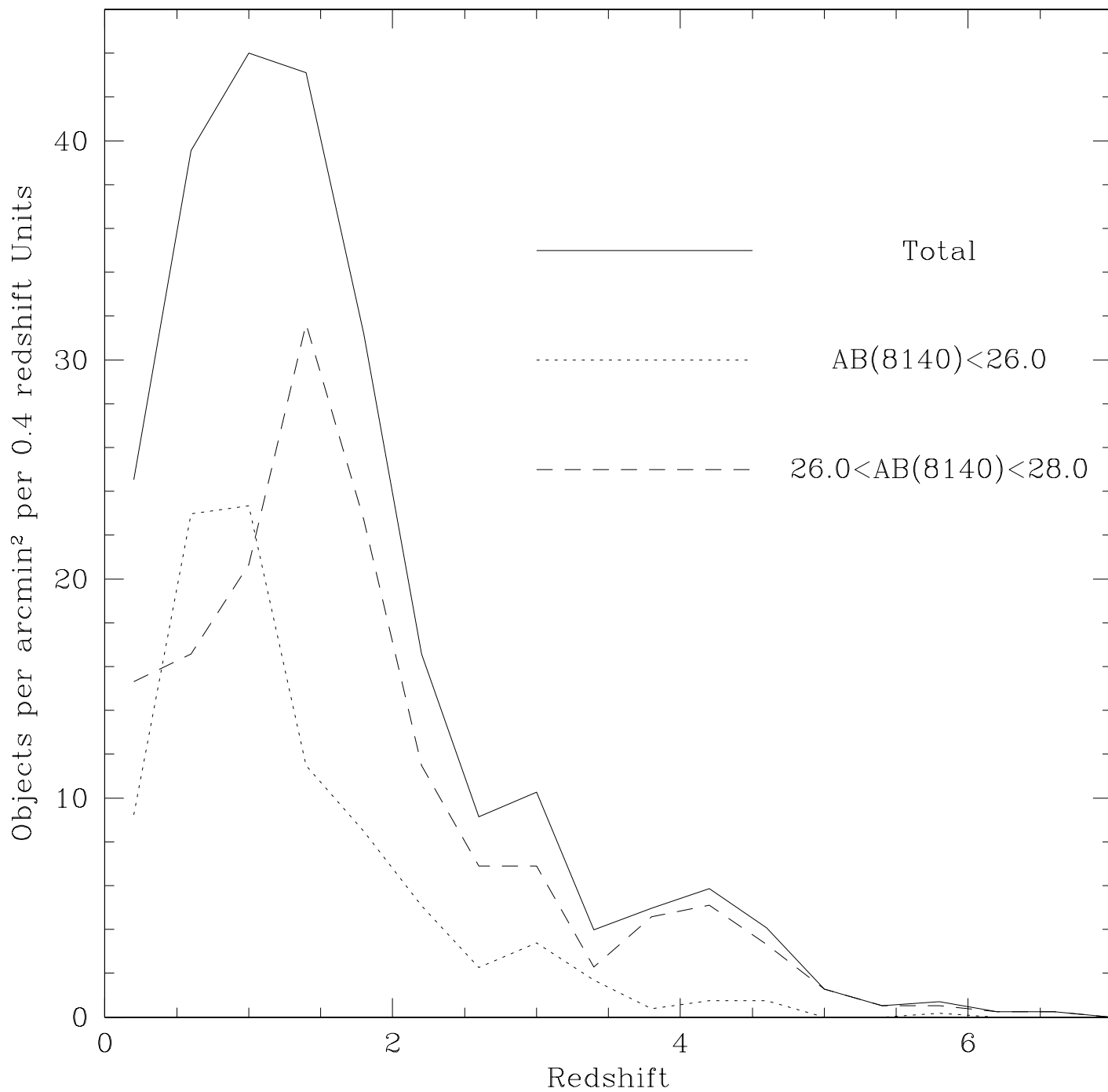


This figure "f8.jpg" is available in "jpg" format from:

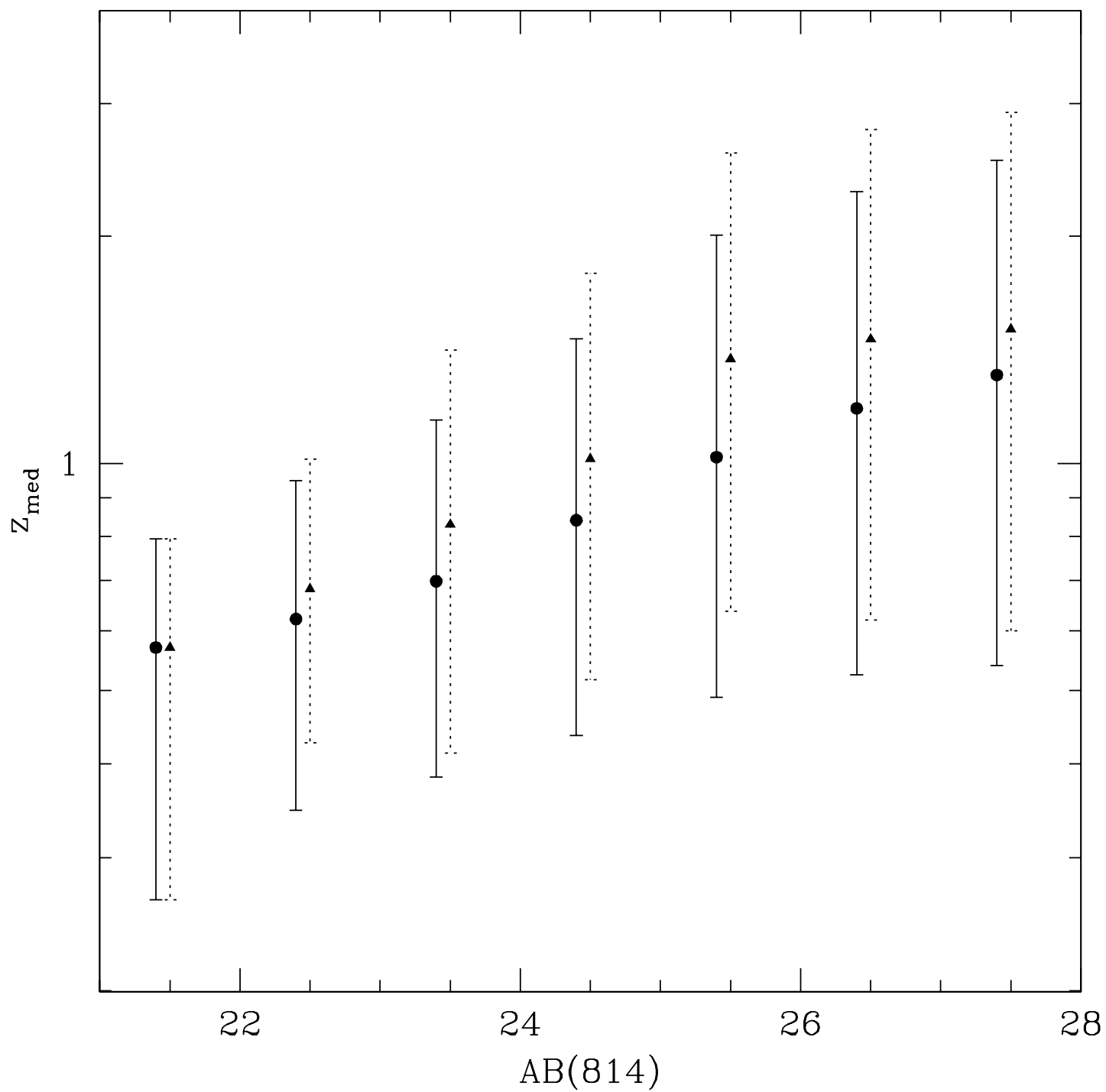
<http://arxiv.org/ps/astro-ph/9809126v1>

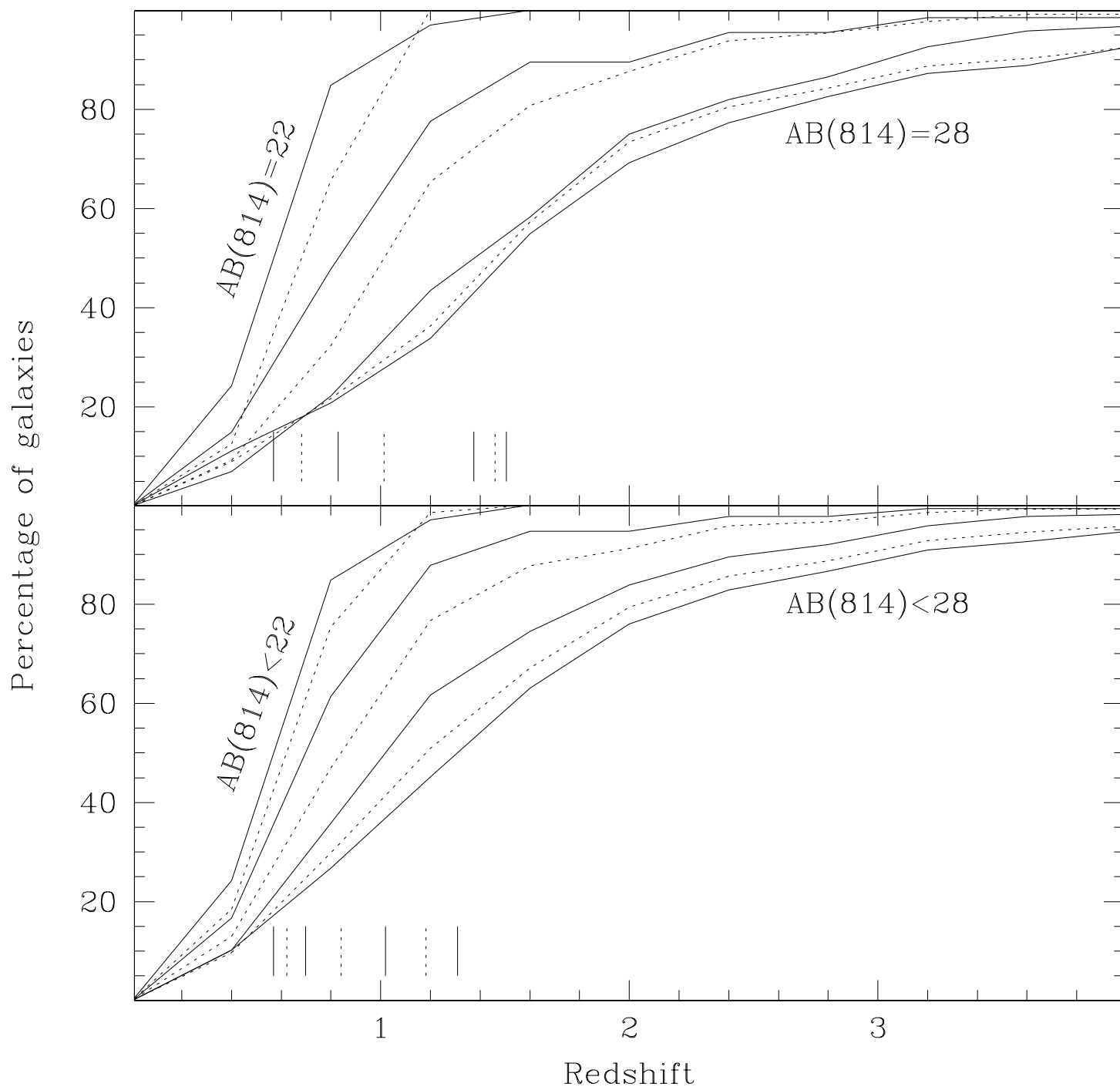












This figure "f14.jpg" is available in "jpg" format from:

<http://arxiv.org/ps/astro-ph/9809126v1>

This figure "f15.jpg" is available in "jpg" format from:

<http://arxiv.org/ps/astro-ph/9809126v1>

